Environment International 177 (2023) 108006

Contents lists available at ScienceDirect

Environment International

journal homepage: www.elsevier.com/locate/envint

Full length article

Towards a better understanding of fine PM sources: Online and offline datasets combination in a single PMF

Marta Via [a,b,*], Jesús Yus-Díez [a,b,1], Francesco Canonaco [c,d], Jean-Eudes Petit [e], Philip Hopke [f,g], Cristina Reche [a], Marco Pandolfi [a], Matic Ivančič [h], Martin Rigler [h], André S.H. Prevôt [c], Xavier Querol [a], Andrés Alastuey [a], María Cruz Minguillón [a]

[a] Institute of Environmental Assessment and Water Research (IDAEA-CSIC), Barcelona 08034, Spain
[b] Department of applied physics, Faculty of Physics, University of Barcelona, Barcelona 08028, Spain
[c] Laboratory of Atmospheric Chemistry, Paul Scherrer Institute, 5232 Villigen PSI, Switzerland
[d] Datalystica Ltd., Park innovAARE, 5234 Villigen, Switzerland
[e] Laboratoire des Sciences du Climat et de l'Environnement (CNRS-CEA-UVSQ), Gif-sur-Yvette, France
[f] Institute for a Sustainable Environment, Clarkson University, Potsdam NY13699, USA
[g] Department of Public Health Sciences, University of Rochester School of Medicine and Dentistry, Rochester NY14642, USA
[h] Aerosol d.o.o., Kamniška 39a, 1000 Ljubljana, Slovenia

ARTICLE INFO

Handling Editor: Marti Nadal

Keywords:
Multi-time resolution
Source apportionment
Submicronic particulate matter
Positive matrix factorisation
PMF
Multilinear engine
SoFi
ME2
Organic sources
Metals

ABSTRACT

Source apportionment (SA) techniques allocate the measured ambient pollutants with their potential source origin; thus, they are a powerful tool for designing air pollution mitigation strategies. Positive Matrix Factorization (PMF) is one of the most widely used SA approaches, and its multi-time resolution (MTR) methodology, which enables mixing different instrument data in their original time resolution, was the focus of this study. One year of co-located measurements in Barcelona, Spain, of non-refractory submicronic particulate matter (NR-PM_1), black carbon (BC) and metals were obtained by a Q-ACSM (Aerodyne Research Inc.), an aethalometer (Aerosol d.o.o.) and fine offline quartz-fibre filters, respectively. These data were combined in a MTR PMF analysis preserving the high time resolution (30 min for the NR-PM_1 and BC, and 24 h every 4th day for the offline samples). The MTR-PMF outcomes were assessed varying the time resolution of the high-resolution data subset and exploring the error weightings of both subsets. The time resolution assessment revealed that averaging the high-resolution data was disadvantageous in terms of model residuals and environmental interpretability. The MTR-PMF resolved eight PM_1 sources: ammonium sulphate + heavy oil combustion (25%), ammonium nitrate + ammonium chloride (17%), aged secondary organic aerosol (SOA) (16%), traffic (14%), biomass burning (9%), fresh SOA (8%), cooking-like organic aerosol (5%), and industry (4%). The MTR-PMF technique identified two more sources relative to the 24 h base case data subset using the same species and four more with respect to the pseudo-conventional approach mimicking offline PMF, indicating that the combination of both high and low TR data is significantly beneficial for SA. Besides the higher number of sources, the MTR-PMF technique has enabled some sources disentanglement compared to the pseudo-conventional and base case PMF as well as the characterisation of their intra-day patterns.

1. Introduction

Air pollution has become one of the most harmful threats to environmental health and climate (Kinney, 2018), being the 4th largest global cause of attributable deaths (Abbafati et al., 2020). Particulate matter (PM) is the pollutant with the highest impacts respect to adverse health effects (WHO, 2021). Identifying and quantifying pollution sources (i.e. source apportionment, SA) has become a major foci in urban air quality research, for which Positive Matrix Factorization (PMF, Paatero and Tapper, (1994)) is one of the most widely used modelling tools (Hopke et al., 2020). Although targeting one pollutant can be effective for specific mitigation strategies, the SA picture is vital

* Corresponding author.
E-mail address: marta.via@idaea.csic.es (M. Via).
[1] now at: Center for Atmospheric Research, University of Nova Gorica, Vipavska 11c, SI-5270 Ajdovščina, Slovenia.

https://doi.org/10.1016/j.envint.2023.108006
Received 13 February 2023; Received in revised form 9 May 2023; Accepted 29 May 2023
Available online 2 June 2023

to improve the understanding of the behaviour of pollution sources. In this broader framework, the multi-time resolution PMF (MTR-PMF) technique represents a handy tool for coupling several groups of species that are measured by different instrumentation and at a different time resolution (TR).

The principles of the MTR-PMF technique were first established by Zhou et al. (2004) with the aim of overcoming the averaging and interpolation practices when combining different TRs (10 min. to 24 h) data subsets. That study was able to retrieve six PM sources coupling data of several TRs, containing repeated and unrepeated species. Also, the study pointed out the higher sensitivity of the novel MTR-PMF technique to missing data in comparison with the regular PMF. Ogulei et al. (2005) used the MTR-PMF to file data gaps with concentration and uncertainty estimations. Subsequently, multiple studies benefitted from this technique, whose highlights will be mentioned hereunder.

The use of the MTR methodology has been applied in diverse inquiries. Kuo et al. (2014) demonstrated that averaging high TR data subsets to low TR data subsets' timestamps could yield the loss of factors with the same experimental data subsets and increased model error. Analogously, Liao et al. (2013) used synthetic data to demonstrate the accuracy of the model to explain the input sources and also found that averaging depreciated the correlation between input and output sources, respect to the MTR technique. Additional results from that work demonstrated that the model is more highly influenced by measurement error modifications than it is by input profile variation. The application of constraints in this work scheme reported beneficial outcomes in terms of the match with the simulated input. The use of constraints was also reported to be advantageous by Crespi et al. (2016), which, moreover, provided solution uncertainty estimation using bootstrap techniques in a constrained MTR-PMF. The use of the MTR methodology by Sofowote et al. (2018) allowed the identification of a source that was causing the major differences in $PM_{2.5}$ concentrations between a pair of nearby sites, traffic and non-traffic. This result was achieved by using several markers measured by different instrumentation leading to more comprehensive model results. In Srivastava et al. (2019), the MTR-PMF application allowed the combination of organic mass spectra and organic species leading to the identification of more factors relative to the standard PMF analysis. Forello et al. (2019) showed that, in addition to retrieving more robust sources MTR-PMF could also enhance the determination of instrumental source-dependent coefficients. This study benefitted from coupling filter samples and aethalometer data to retrieve the source dependent absorption Ångström exponent values and their variability without *a priori* assumptions.

Other studies have not used the MTR technique but instead have focused on coupling different instrument data subsets with the same TR and assessing the robustness of the outcomes depending on the subsets weightings (Crippa et al., 2013; Slowik et al., 2010a). Slowik et al. (2010b) reported that the uncertainty unbalance when coupling data from two different instruments can lead to unevenly representation of a data subset since there may be stronger internal correlations in one set versus the other. For example, in AMS data, there are characteristic m/z patterns due to the fragmentation process. This decompensation of the instruments' representation was tested by relatively changing the weighting of the uncertainty matrix of one of the instruments and assessing the scaled residuals. This work found that the solution with the lowest scaled residual means was obtained with a weighting of the PTR-MS dataset by 0.7 for winter and 0.8 for summer without changing the AMS dataset weight. Moreover, Belis et al. (2019) tuned the weighting of the instrumentally-established errors to provide the receptor model with optimum weighting for each instrumentation's data. This study proposed to adjust the weights according to the scaled residuals and Q/Q_{exp} outcomes. Thereupon, Tong et al. (2022) further explored the combination of two different instrumentation datasets by weighting their errors and assessing the outcomes by analysing the intersection between both datasets' scaled residuals histograms. That study showed that the most balanced solutions were found for weightings close to unity (scant weighting).

The origins of submicron aerosol in Barcelona have been previously studied with a wide variety of instrumentation. Most of the studies are based on measurements with a TR of 24 h and with organic aerosol (OA) as a bulk species (Pérez et al., 2008; Brines et al., 2019; In't Veld et al., 2021). Pérez et al. (2008) reported seven groups of pollutants classified by their major origin for the bulk PM_1 based on chemical analysis of offline PM_1 filter samples: Organic Matter (OM) + Elemental Carbon (EC), sea spray, crustal, ammonium, sulphate and nitrate. Similarly, In't Veld et al. (2021) identified heavy oil combustion, vehicle exhaust, non-emission vehicle emissions and a metallurgical industrial source in a 9-years, multi-site $PM_{2.5}$ time series. Brines et al. (2019) and Minguillón et al. (2012) performed SAs joining daily organic and inorganic species concentrations from offline PM_1 filter samples that yielded to better source descriptions. Regarding OA, high TR OA mass spectra PMF led to the identification of sources consisting of cooking-like OA (COA), hydrocarbon-like OA (HOA, attributed to road traffic), biomass burning OA (BBOA), and two oxygenated OA differentiated into a Less and a More Oxidised state (LO-OOA, MO-OOA) (Mohr et al., 2012; Minguillón et al., 2016; Via et al., 2021). The next step towards an optimal SA would be to couple this wide variety of species with the highest possible TR in order to characterise the intra-day variability of these sources. The MTR-PMF technique allows for SA of data subsets with different TR to provide an improved description of the sources in terms of the contribution of a wider range of species and their time variation.

The objective of the present study is twofold. It pursues in a better quantitative SA of the submicron aerosol sources, identifying different organic and inorganic soluble ions' together with black carbon (BC) and metal species, leading to a more complete source quantification and to the identification of additional potential sources. The submicron PM components used for this aim were: i. organic aerosol (OA), measured by a Quadrupole Aerosol Chemical Speciation Monitor (Q-ACSM); ii. non-refractory secondary inorganic species (SIA), including SO_4^{2-}, NO_3^-, NH_4^+, and Cl^-, also measured by a Q-ACSM; iii. BC measured by an aethalometer; iv. elemental species, from filter samples collected by high-volume samplers and analysed via ICP-AES and ICP-MS. This study also aims to examine the effect of the averaging of the high resolution (HR) data subset and of the uncertainty weighting of the datasets towards the reliance of MTR-PMF results. This parameter optimisation will provide guidance for future MTR-PMF users who seek for the optimal combined SA. To the authors' knowledge, this work provides the first study of these two parameter effects in a coupled manner from an analytical perspective to obtain the best possible SA of the submicronic aerosol.

2. Methodology

2.1. Sampling site, period and instrumentation

Measurements were performed at the Palau Reial site (PR; 41° 23′ 15″ N; 02° 07′ 05″ E; 80 m a.s.l.), an urban background site located in NW Barcelona near one of the busiest avenues of Barcelona (Diagonal Avenue, Fig. S1). More details of this site can be found in Minguillón et al. (2016) and Pey et al. (2010). The sampling period was from September 2017 to October 2018. The results from the deployed Q-ACSM and the aethalometer AE33 have been reported in Via et al. (2021), Yus-Díez et al. (2021). High volume samplers were co-located and used to collect PM_1 filter samples, as described in In't Veld et al. (2021). The combination of these three datasets has been prepared as input to PMF model both separately and for MTR-PMF.

2.1.1. Q-ACSM measurements

A Q-ACSM (Aerodyne Research Inc.) was deployed to measure NR-PM_1 particles between 75 and 650 nm. Particles are flash-vaporized at 600 °C in high vacuum conditions and ionized by hard-electron impact (70 eV), and the resulting fragments are analysed by a quadrupole mass

spectrometer (Ng et al., 2011). A fragmentation table (Allan et al., 2004) is used to convert the signal spectra into organic aerosol or inorganic species concentrations. An OA matrix with concentrations of unit mass resolution species (*m/z* from 12 to 120 Th) was generated. Ionization Efficiency (IE) and Relative Ion Efficiency (RIE) calibrations were conducted using 300-nm monodispersed NH_4NO_3 and $(NH_4)_2SO_4$ particles (Ng et al., 2011). The collection efficiency correction was applied according to Middlebrook et al. (2012), with CE values ranging 0.50–0.99. More details on calibration, settings and corrections can be found in Via et al. (2021). The OA uncertainty matrix was calculated as described by Ulbrich et al. (2009). The NR-PM_1 inorganic species' uncertainties were calculated as in Crenn et al. (2015). A thorough inspection of the signal-to-noise ratio of the input matrices was performed and all species were found in a sensitive range of 2–15. Also, the *m/z* range was upper-limited to 100 *m/z* as the mass of those ions between 100 and 120 only accounted for a 6% on average.

2.1.2. Aethalometer measurements

BC measurements were performed through an AE33 multi-wavelength Aethalometer (model AE33, Magee Scientific, Aerosol d.o.o.; Drinovec et al., 2015) with a PM_1 cut-off inlet. The AE33 is based on the measurement of light transmission at seven wavelengths (370, 470, 520, 590, 660, 880 and 950 nm) through two sample spots with different flows and particle loading relative to the reference spot. The aethalometer filter loading effect was corrected online by the dual-spot manufacturer correction (Drinovec et al., 2015), and the multiple scattering correction constant, C, was set to 2.44, as reported by Yus-Díez et al., (2021). The absorption Ångström exponents (α) for liquid fuel and solid fuel were set $\alpha_{lf} = 1$ and $\alpha_{sf} = 2$, respectively, as a rounding of the 0.9, 1.68, respectively, from Zotter et al. (2017). Posteriorly, the speciation of the BC regarding its origin into liquid fuel (BC_{lf}) and solid fuel (BC_{sf}) was obtained by applying the Sandradewi model (Sandradewi et al., 2008) to these BC measurements. The measurement uncertainty for the absorption was set to 15% of the measurement (Forello et al., 2019) for each of the seven wavelengths absorption. Error propagation was used for obtaining the uncertainty estimation of BC_{lf} and BC_{sf}. The data, generated at a 1-minute TR, was averaged into the 30-minute timestamps matching the Q-ACSM data to provide homogenised measurements. The ensemble of Q-ACSM (OA matrix and SIA) and aethalometer data (BC_{lf}, BC_{sf}) will be hereinafter referred to as the high time resolution (HR) data subset.

2.1.3. Offline measurements

A total of 83 PM_1 samples were collected at PR during the sampling period on 150 mm quartz micro-fibre filters (Pallflex 2500 QAT-UP) using high-volume samplers (DIGITEL DH80 at 30 $m^3 \cdot h^{-1}$) with a frequency of 1 out of 4 days. These 24-h (midnight-to-midnight) samples were divided into four portions to perform different analytical protocols on each. A quarter of each sample was acid digested and subsequently analysed by Inductively Coupled Plasma Optical Emission Spectrometry (ICP-OES, ICAP 6500, THERMO Scientific) and Inductively Coupled Plasma Mass Spectrometry (ICP-MS, X Series II, THERMO Electron Corporation) for the determination of major and trace element concentrations, respectively (procedure by Querol et al. (2001)). These results are summarised in In't Veld et al. (2021) and Via et al. (2021). Another quarter of each sample was water extracted and analyzed by ion chromatography for the determination of SO_4^{2-}, NO_3^-, and Cl^- concentrations and by selective electrode for the determination of NH_4^+ concentrations. A portion of the filter was analyzed by a thermal-optical method (Sunset OCEC analyser, Sunset Laboratory Inc.) following the EUSAAR2 protocol (Cavalli et al., 2010) for the EC and OC concentrations determination. The uncertainty of these measurements was calculated as described in Escrig et al., (2009). These species will be referred to as the low TR (LR) data subset.

2.2. Combination of data subsets

To prepare the input for the PMF model to be applied and achieve PM_1 mass closure, the following criteria were applied:

i. The concentrations of the species analysed by more than one technique were cross-validated, and the technique with higher TR was included for the final data set. Hence, concentrations of SO_4^{2-}, NO_3^-, NH_4^+, and Cl^- used are those from Q-ACSM after validating them against filter samples concentrations (Via et al., 2021). OA concentrations from Q-ACSM were compared and discussed with OC measurements from filter samples in Via et al. (2021) (here summarised in Table S1), and in the same way, BC concentrations from aethalometer were compared to measurements of EC from filter samples (Fig. S2); ii. The species with a signal-to-noise between 0.2 and 2 (so called weak) were kept after multiplying their uncertainties by a factor of two (Table S2).

Therefore, the HR data subset includes OA mass spectra from *m/z12* to *m/z100*, SO_4^{2-}, NO_3^-, NH_4^+, and Cl^-, and BC_{sf} and BC_{lf} (17603 datapoints); and the LR data subset comprises Ca, Al, K, Mg, Na, Ti, V, Cr, Mn, Co, Ni, Cu, Zn, As, Sn, Sb, and Pb (83 datapoints). The number of species and samples of the LR data subset provides a number of degrees of freedom per variable (72) in the 50–100 advised range (Henry et al., 1984). The elements selection was based on their signal-to-noise ratio values (0.5 threshold) and stability throughout the period.

2.3. Positive matrix factorisation analysis

2.3.1. Multi-time resolution PMF theoretical frame

When utilising subsets with different TRs, the data should be prepared in a specific manner. The diagram shown in Fig. 1 elucidates the input data disposition to be fed to the model in the present study. The PMF mass balance equation needs to be modified as in Zhou et al. (2004):

$$x_{sj} = \frac{1}{t_{s2} - t_{S1} + 1} \sum_{k=1}^{P} f_{kj} \sum_{i=t_{S1}}^{t_{s2}} g_{ik} \eta_{jm} + e_{sj} \quad (1)$$

where *s* indicates the sample, t_{s1} and t_{s2} are the starting and ending time points for the *s*th sample and η_{jm} are adjustment factors for replicated species in different TR or measured with different analytical methods (represented by the subscript *m*). In this study, η_{jm} equals to 1 in all cases coherently with the decision not to include replicated species.

The Multi-linear Engine 2 (ME-2) (Paatero, 1999) was applied to solve this problem through the Source Finder software (SoFi Pro, v8.0.4, Datalystica Ltd., Villigen, Switzerland, Canonaco et al. (2021)), within the Igor Pro software environment (Wavemetrics, Inc., Portland, OR, USA).

2.3.2. Instrument weighting

In order to generate sensible SA results, a fair representation of all

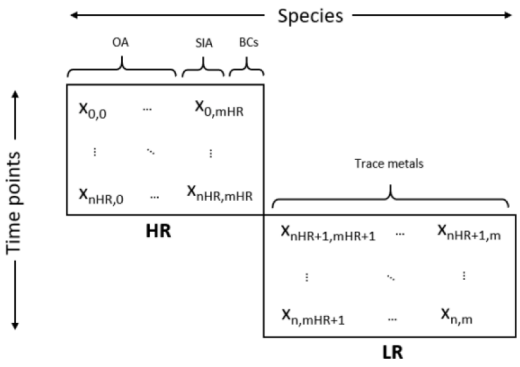

Fig. 1. Schematic of the combination of the High Resolution (HR) and Low Resolution (LR) subsets input matrix (X) for MTR-PMF.

species and groups of them must be ensured. Although the signal-to-noise ratio (Table S2) is comparable from one data subset to the other, the datasets can be uncertainty-unbalanced. An approach to evaluate the fairest uncertainty weighting is the assessment of the resulting PMF ratio of the error (e_{ij}) over the extent on which a measurement (x_{ij}) can be varied (σ_{ij}), i.e., scaled residuals. The instrument-individual uncertainty adjustment has been widely used for balancing these species' scaled residuals (Sofowote et al., 2018), which are expected to have a Gaussian distribution centred to zero (Zhou et al., 2004). However, less attention has been paid to the ensemble of all scaled residuals, which can lead to non-unimodal distributions especially if different instrumentation data is put together. A balanced PMF solution has been defined as that whose magnitude of scaled residuals is independent of the instrument (Slowik et al., 2010a). Thus, the scaled residuals distribution should be unimodal. Tong et al. (2022) showed that even for signal-to-noise-balanced input matrices and equally internally correlated ions within subsets, PMF residuals can be affected by the relative number of species included in each subset.

To address this inherent unbalanced coupling of different instrument data, weighting each subset has been proven successful (Crippa et al., 2013; Tong et al., 2022). The quantity C represents the scaling value for each of the data subsets' uncertainties (σ). In this study case, these Cs will be hereinafter called C_{HR} and C_{LR}, for the HR and LR datasets, respectively:

$$\sigma_{ij}^{HR'} = \frac{\sigma_{ij}^{HR}}{C_{HR}}, \quad \sigma_{ij}^{LR'} = \frac{\sigma_{ij}^{LR}}{C_{LR}} \tag{2}$$

The optimality assessment of a weighted PMF solution will be based on the similarity of the scaled residuals with those from PMF of the separate subsets. The quantification of this similarity among the data subsets scaled residuals was proposed by Tong et al. (2022), assessing the overlap between the histograms of the scaled residuals of the different subsets, in this case, HR and LR (example depicted in Figure S3). This quantity can be calculated by:

$$F_{overlap} = \int_{-a}^{a} \min\left[P_{HR}(s_{ij}), P_{LR}(s_{ij})\right] \tag{3}$$

where P_{HR} and P_{LR} indicate the density of probability of occurrence of the scaled residuals value s_{ij}, and a represents the integration limits. This integral is expected to cover the [0,1] range, being the extremes of this interval the null and full intersection, respectively. Defining $F^*_{overlap}$ as the overlap of the scaled residuals histograms of the independent HR and LR PMFs, the optimal solution is, as defined in Tong et al. (2022), the one which best fulfills the condition

$$F_{overlap}(C_{HR}, C_{LR}) \; F^*_{overlap} \tag{4}$$

In this study, the number of bins and the threshold range was set to 100 and 50, respectively, since these parameter values provide a wide and reasonable range of histogram intersection values. Note that the numerical integration has been tackled by means of the trapezoid integration method, which is expected to incorporate estimation errors.

2.3.3. Workflow design

With the purpose of assessing the MTR output sensitivity to the TR averaging and uncertainty weighting effects, a multi-approach procedure was designed, similarly to Belis et al. (2019).

Approach 1. HR SA. SA was performed to a data subset including the OA mass spectra, SIA species, and BC measurements separated into BC_{lf} and BC_{sf}. The TR of this data subset is 30 min.

Approach 2. LR SA. SA was performed on the data subset that contains metals concentrations at a TR of 24 h every four days.

Approach 3. Pseudo-conventional SA. SA was performed on a data subset that contains the metals, the SIA from Q-ACSM, and the BC and the OA as a bulk, all averaged to the LR data subset timestamps (24 h every four days). The BC was introduced as a species summing BC_{lf} and BC_{sf}, and the OA as the sum of all its *m/z*s to mimic the EC, OC concentrations that a conventional offline data subset would account for. Thus, the 'pseudo-conventional' naming refers to the mimicking of this data coupling to a conventional offline approach. This approach provides the reference to compare the posterior MT-PMF results with this conventional offline precursor SA methodology.

Approach 4. Base case SA. SA was performed on a data subset containing the HR data subset averaged to the LR subset timestamps (24 h every four days) and the LR data subset so that both data subsets are run under the same TR. This Approach does not apply uncertainty weightings. This data subset represents the most basic ensemble the MTR-PMF more refined results can be compared with.

Approach 5. MTR-PMF. SA performed on the dataset including OA species, SIA compounds, BC_{lf}, BC_{sf}, and metals in their native TR using the MTR-PMF technique. This data coupling requires performing first TR and C weightings assessment in order to find the most effective settings for both mathematical and environmental adequacy of the results. The determination of the highest suitability of these parameters' values was based on the scaled residuals histogram intersection between subsets. Whilst the resolution of the LR dataset remains constant (24 h every 4 days), the HR subset is averaged to different resolutions (R_1, referring to the TR of the HR dataset): R_1 = 30 min., 1 h, 2 h, 3 h, 6 h, 12 h, 24 h. Weighting scaling values combinations are: (C_{HR}, C_{LR})=(1,0.001), (1,0.01), (1,0.1), (1,1), (1,10), (0.001,1), (0.01,1), (0.1,1), (10,1), (100,1), (1000,1). The C-weightings testing experiment was afterwards repeated in a narrower range of C-values amongst the determined best combinations resulting in optimal resolution. Once the best R_1 and C_{HR}, C_{LR} parameters are found, standard SA is performed on this data subset with the optimised parameters. These results are then compared to those from Approaches 1, 2, 3, 4.

2.4. PMF settings and post-PMF data curation

Although a *rolling* PMF is a more convenient methodology with respect to the *seasonal* PMF as reported in Via et al. (2022), in this study, in which the TRs are so different and both datasets include multiple gaps, it would lead to different representation of each subsets because each has different number of points of each. To avoid this issue, PMF was run across the whole period. Constraints were not applied to allow the model to freely adapt the mass proportions of both subsets. The lack of similar studies that couple OA mass spectra, SIA, BC types and metals precludes availability of reference profiles. The application of constraints through anchor profiles would require the *a-priori* estimation of the mass proportion between LR and HR species for a given source, while this result is in fact one of the expected outputs of the present study newly applied methodology.

PMF was run in each of the aforementioned Approaches 10 times per number of factors so that the solution space is explored and the user can select the most physically reasonable solutions. To treat the unconstrained, and therefore, unsorted number of runs generated, an unsupervised non-hierarchical clustering technique was adopted. This method was applied after PMF, providing *k* profiles as a result of the average of all profiles within the same given cluster (more details are provided in SI Section B). The time series, explained variations and relative concentrations etc. associated to each profile were averaged within those belonging to the same profile cluster. In this way, the PMF solutions consisted of distinct, stable mean profiles and time series with their standard deviations amongst all cluster members. The k-means clustering algorithm was applied under the SciPy library environment in Python.

The SA error assessment methodology and results are extensively discussed in SI section D, including the rotational and clustering errors.

3. Results and discussion

3.1. Independent PMF

SA is performed on the different TR subsets separately, this is, the aforementioned Approach 1 and Approach 2. Their objective is to calculate the scaled residuals histogram overlap of the independent data subsets ($F^*_{overlap}$) as in Tong et al. (2022). The Approach 1 results, responding to the HR subset SA, are shortly described hereinunder and in Figure S4 and briefly here. Regarding the LR data subset SA (Approach 2), the results are not a self-explanatory SA solution since information provided by the species is limited and they only represent a 2% of the bulk PM_1 mass. However, an environmentally reasonable solution was obtained, whose scaled residuals are later used for the $F^*_{overlap}$ calculation (Eq. (3). The detailed solution is presented in the SI Section C and Figure S5.

The Approach 1 results already represent an improvement with respect to the OA SA, which led to the identification of five OA sources: HOA, COA, BBOA, LO-OOA and MO-OOA as reported by Via et al. (2021). The addition of the inorganic NR-PM_1 and BC species already proved advantageous in Zografou et al. (2022) by identifying an additional factor. Similarly, the present SA solution consists of 6 factors, 3 purely primary, 2 secondary and a potentially mixed factor (Figure S4). The mass closure of this SA shows a 12% of underestimation of the input concentrations (Fig. S4c).

The major source is the aged aerosol + ammonium sulphate (AS) factor (34%, Fig. S4d), which has a high *m/z44*-to-*m/z43* ratio, indicator of secondary organic aerosol (SOA) aging (Figs. S4a, S4d). Its diel cycle (Fig. S4e) shows an increase during the hours of maximum insolation, oppositely to the fresh OA factors since the production or reception of this source counteracted the boundary layer thickening and enhanced breeze effects. The fresher SOA is split in two factors, the fresh SOA + ammonium nitrate (AN) + ammonium chloride (ACl) and the fresh OA + Industry (Fig. S4a), considered to be actually different as they present uncorrelated time series ($R^2 = 0.06$) and different intra-annual variation (Fig. S4b). The Fresh SOA + AN + ACl source represents a 16% of the total PM mass (Fig. S4d). This factor comprises LO-OOA and almost all of the AN and ACl concentrations. It is minimal in summer and a significantly decreases during higher wind and boundary layer conditions (Fig. S4e). The Fresh SOA + Industry source represents a 14% of the output mass (Fig. S4d). The industrial contribution was not identified for this subset in previous studies, but here it was recognised by the presence of its marker *m/z58* and *m/z86* (Passig et al., 2021). These two ions are markers of amines, likely from industrial activities (Ge et al., 2011). However, this profile is LO-OOA-like since this OA factor accounts for most of the mass (Fig. S4a). This source, which presents a mix of primary and secondary species, was higher during the summer months due to the enhancement of the photo-oxidation of SOA precursors and presents a minimum during breeze-entrance hours (Fig S4e). However, it remains constant during morning as if the widening of the boundary layer was being counteracted by the enhancement of this source as a likely consequence of either the arrival of industrial plumes or the rate of SOA formation. The traffic source (16%, Fig S4d) showed the typical hydrocarbon-like OA features and is tightly linked to the BC_{lf} emissions (Fig. S4a). This source contribution is lower in summer months and its diel cycle is coherent with rush hours of the congested avenue near the site (Fig. S4e). Biomass burning is clearly identified by both the *m/z* markers and the BC_{sf} in the source profile (Fig. S4a), and it represented 13% of the modelled mass (Fig. S4d), with, as expected, significantly higher concentrations in cold periods and in evening hours (Fig. S4e). The cooking-like OA source (7%, Fig. S4e) is mixed with sulphate and BC_{lf}, indicating that this is not a pure cooking factor, but a mixture of multiple sources containing cooking marker ions, such as *m/z55* and *m/z41*, as already described in Via et al., (2021) (Fig. S4a). The diel cycle peaked right before cooking times in Barcelona and was essential to identify this factor (Fig. S4e). The large peaks for most sources in August (Fig. S4e) were attributed to the limited data availability in this month (four days) which lead to unrepresentative results relative to the other measurement periods. The data availability data can be seen in the second plot of Figure S1 in the SI of Via et al. (2021).

3.2. PMF applied to an equivalent pseudo-conventional data subset

The Approach 3 was based on the analysis of the hereinafter called pseudo-conventional data subset, consisting on those species which are used in offline SA (Amato et al., 2016; In't Veld et al., 2021): metals, SIA and the EC and OC (some studies use organic tracers as well, but these are not available for the current data subset). The aim of this SA is to provide a reference solution mimicking one without the high TR data to prove or discard the added value of the MTR-PMF. The data subset has been built with a 24-hours TR, averaging those species of originally higher TR. However, this approach does not result in very good results since its mass closure (Fig. S6c) shows an output underestimation of a 47%. This weak agreement closure could be related to the many gaps encountered in the OA and BC time series averaged to the LR timestamps.

The pseudo-conventional data subset SA provided 4 PM_1 sources: AN + biomass burning (36%), AS + heavy-oil combustion (28%), industry (28%) and road dust (8%) (Fig. S6d). The AN + biomass burning profile contains high proportion of NO_3^-, Cl^-, NH_4^+, and K as its main contributors, and represented approximately a 20% of the OA and BC mass (Fig. S6a). Its contribution was higher during cold months (Fig. S6b), being the August peak disregarded due to its low representativeness. The AS + heavy oil combustion is characterised by the V, Ni, Co, Mg elements and high SO_4^{2-} and NH_4^+ contributions, and it contains a small fraction of OA and EC (~15%) (Fig. S6a). It is higher during summer months as expected from SO_4^{2-} concentrations as seen in Figure S6b. The industry factor contains a ~ 30% of the organic mass, and several markers arising from industrial activities: Pb, As, Cd, Cr, Ni, etc (Fig. S6a). This factor does not present a substantial seasonal trend (Fig. S6b). The road traffic factor contains high concentrations of Mn, Cu, Zn, Sn, and Sb, all of them related to non-exhaust emissions; and substantial OA and EC, related to traffic-exhaust emissions (Fig. S6a). This factor presents a subtle seasonality, decreasing in the warm period due to the holiday-related traffic intensity drop and greater vertical mixing during daytime in those months (Fig S6b).

3.3. Base case for MTR-PMF

Approach 4 provided a SA of a regular PMF applied to the data subset built with all available species averaged to the lowest TR, i.e., 24-hours. No C weights ($C_{HR} = 1$, $C_{LR} = 1$) were applied during the model running. This solution will be used to evaluate the improvement resulting from the MTR-PMF application with optimised parameters. The mass closure plot (Fig. S7c) reports only a 9% underestimation of the input mass.

The SA resolved 6 PM_1 sources: Aged SOA + AS (31%), Fresh SOA + AN (26%), Heavy oil combustion (15%), Traffic (13%), Biomass Burning + Mineral (12%) and Road Dust + Industry (4%) (Fig. S7d). The number of factors is the same as that of HR data subset SA, even if the metal species were added. Nevertheless, some mixing in sources was acknowledged. For instance, the Fresh SOA + AN, which also included *m/z60, m/z73* and BC_{sf}, markers of biomass burning (Fig. S7a), even though both sources' time series are distinct enough (Fig. S7b). Another explanation for this mixing could be that the reported SOA is formed from biomass burning emissions.

3.4. MTR-PMF sensitivity to R_1 and C values

Approach 5 explores the optimal HR data subset TR and the uncertainty weights combination for the MTR-PMF analysis before proceeding with the final SA solution exploration. The number of factors of the solutions is not assessed in the parameter evaluation but in the solution

assessment (following section 3.5), which was not evaluated mathematically but with the aim to provide an environmentally interpretable sense. Hence, MTR-PMF was run for 6–8 factors for each combination of TR and (C_{HR}, C_{LR}). Although 13 C_{HR}, C_{LR} combinations were set when launching the model, not all of them produced reasonable results (or not for all resolutions) due to the model's inability to process those weighted matrices. This result was found for (C_{HR}, C_{LR}) = (1,100), (1000,1). Once this first broad scan of C values was done, another C-value analysis covering a narrower range was performed to find the most feasible combination.

3.4.1. Scaled residuals overlap

The first step in this analysis was to examine the scaled residuals of both data subsets when coupled into the MTR-PMF. Figure S8 shows the means and standard deviations of all C value combinations for HR and LR including all the TR runs. This plot assesses both the magnitude of the scaled residuals and their stability, which is severely compromised in the C combinations of (0.01,1), (0.001,1). These combinations enlarging the HR uncertainties result in a LR data subset scaled residuals increase. In terms of centrality, some C combinations present means systematically above zero, especially for the LR subset. Those C value combinations whose medians are less zero-displaced were the (1,1), (0.1,1), (0.01), (1,10), (1,1). However, some of their means were out of the range of the plots for the LR data subset, indicating the inclusion of significative outliers.

The calculation of the HR, LR histogram overlap is a powerful metric to assess the coupling of both subsets. The intersection between histograms from the standalone solutions for HR and LR (F*, eqs. (3), 4), is shown in Fig. 2. It shows an overlap of 43.4% for the 100 bins and in a range of scaled residuals of [-50,50]. Fig. 3 shows the histogram intersection of the HR and LR subsets in the resulting MTR-PMF for 100 bins and range of scaled residuals in the [-50,50] range, for all the R_1 and C combinations under study. This plot shows a maximum in the histogram intersection at 6 h C= (1, 10), but is inconsistent with similar Cs or resolutions. Therefore, it was considered as an outlier. There is a slight trend in which the higher TRs present higher histogram overlaps. Hence, R_1 = 30 min resolution will be that selected for further study. Amongst C values, the histogram overlap grows towards those combinations that reduced (increased) HR (LR) uncertainties, this is, those that make LR species weaker with respect to HR species in terms of signal-to-noise. Contrarily, the 24 h TR subset presents higher and decent histogram intersections for those C combinations which decrease the relevance of HR species. This behaviour can be described as follows: when the MTR-PMF is launched with very different number of timestamps and species, the metal species might be difficult to assimilate by the model and therefore they need to be downweighted respect to the HR ones. Nevertheless, when both subsets' TRs are more similar, the model allows

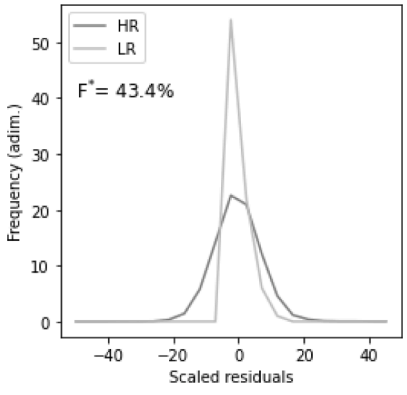

Fig. 2. Scaled residual normalized histogram intersection for the standalone HR and LR PMF results. The histogram overlap (F*) is shown in percentage in the upper left.

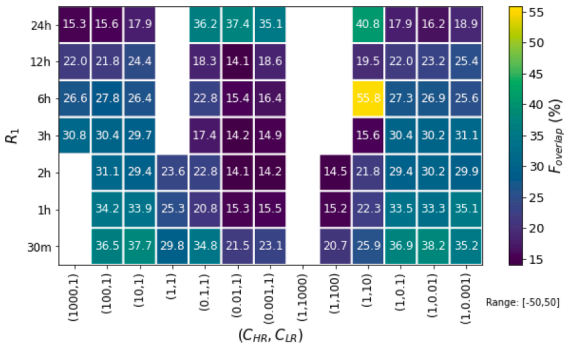

Fig. 3. Heatmap of scaled residual histogram overlap for HR, LR subsets for the range of data between (-50, 50) for each R_1, Cs combinations.

the LR class of species governate the PMF solution.

Fig. 4 shows the histogram intersection of all runs of R_1 = 30 min and for all the C-values and the mean and the standard deviation of all the repeats for each C combination. In Fig. 4a, the C-value combinations range is large and the (1,1), (1,0.1), (1,0.01), (1,0.001), (10,1) and (100,1) seem the best compromise between maximisation and stability. Taking the three highest values (all above the 30%, Fig. 4a), PMF has been re-run amongst these values and the analogous plot is shown in Fig. 4b. In this one, the highest overlap which also presents stability is the combination of (C_{HR}, C_{LR}) = (1,2). This set divides the LR uncertainties by 2. Nonetheless, even though these weightings are those which maximise the $F_{overlap}$, those runs of similar $F_{overlap}$ ($F_{overlap}$ > 30%) were also explored. The run that better explained the site pollution sources was that of (C_{HR}, C_{LR}) = (1,5) as justified in SI section E. Hence, weightings of (C_{HR}, C_{LR}) = (1,5) will be used in Approach 5.

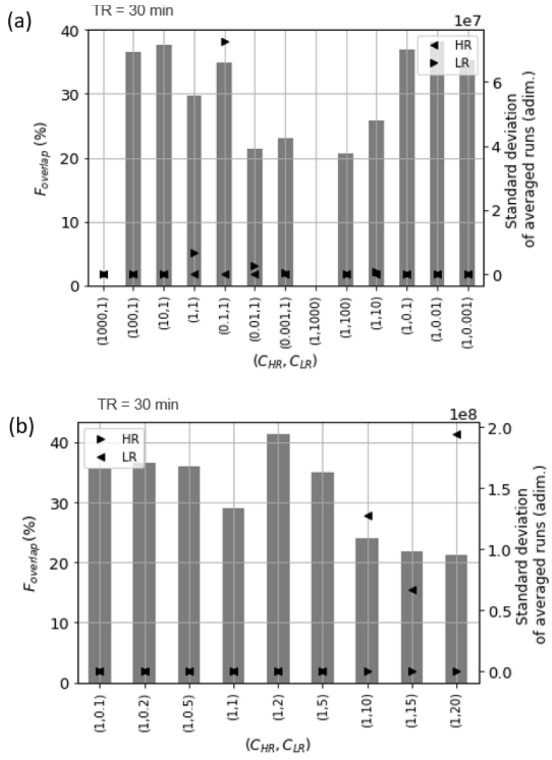

Fig. 4. Scaled residual histogram overlap, F*, for both subsets for the range of data of [-50,50] for each 30-minute C_{HR}, C_{LR}, combination (bars). Standard deviation (triangles) of residuals is shown for the standard C values exploration (top) and the narrower range exploration (bottom).

3.4.2. Q residuals

The normalised Q residuals, this is Q/Q_{exp}, were analysed R_1-wise. Each include all C value combinations. Fig. 5 shows that the 30 min Q/Q_{exp} median value is the only one above one (1.01), indicating hence that the overall fit is better than expected based on the uncertainty of the measurements. However, its values above median are small, indicating hence that there is not a systematic underestimation of the uncertainties. Contrarily, the fact that other R_1 results had medians below 1 indicate that the uncertainties were overestimated. Hence, this Q/Q_{exp} assessment supports the choice of 30 min as the best R_1 to which perform SA.

3.5. Multi-time resolution PMF source apportionment

The SA for the MTR subset, containing both HR and LR data in their original timestamps (30 min and 24 h every four days) and with uncertainty weights of $C_{HR} = 1$, $C_{LR} = 2$ (Approach 5) is shown in Figs. 6, 7. Solutions with ± 1 factor were also evaluated and disregarded due to less resolved or interpretable profiles (Fig. S9). Figs. 6 and 7 show the 8 PM_1 sources retrieved: AS + heavy oil combustion (25%), AN + ACl (17%), aged SOA (16%), traffic (14%), biomass burning (9%), fresh SOA (8%), COA (5%), and industry (4%) (Fig. 7d). The mass closure of the bulk PM_1 shows good agreement with a 12% of underestimation of the input measurements (Fig. 7c).

AS + heavy oil combustion. The AS + heavy oil combustion presents high concentrations of SO_4^{2-} and NH_4^+ (AS), and V, Ni, Co, corresponding to heavy oil combustion emissions from shipping activities (Fig. 7a) (Caumette et al., 2009; Corbin et al., 2018). More than a 50% and a 35% of the SO_4^{2-} and the NH_4^+, respectively, are attributed to this source (Fig. 6). A 24% of the mass of this factor is attributed to a MO-OOA factor (Fig. 7a). A combination of these sources was reported for the offline SA in Brines et al. (2019). This profile is consistent with the result obtained in Approach 1, where the MO-OOA + AS was also the highest contributor to the total mass. Heavy oil emissions intercepted are both locally emitted and long range transported from the shipping of the Mediterranean, carrying AS (a combination of direct SO_3 emissions (Agrawal et al., 2009) and oxidised SO_2 emissions) and aged SOA. This factor time series was enhanced in summer and its diel presents a growth around midday (especially in summer, Fig. 7e), both phenomena related to: i. the higher photochemical conversion rate of SO_2 into SO_4^{2-} in the summer season (Hidy, 1994); ii. stronger sea breeze development in warm months after noon carrying marine aerosol and aged recirculating pollutants; iii. greater photochemistry promotion at the months/hours of maximum insolation, promoting SO_2 and DMS oxidation into sulphates; iv. increase of the shipping activity in summer (Pérez et al., 2016); v. lower air mass renewal in summer (Gangoiti et al., 2001).

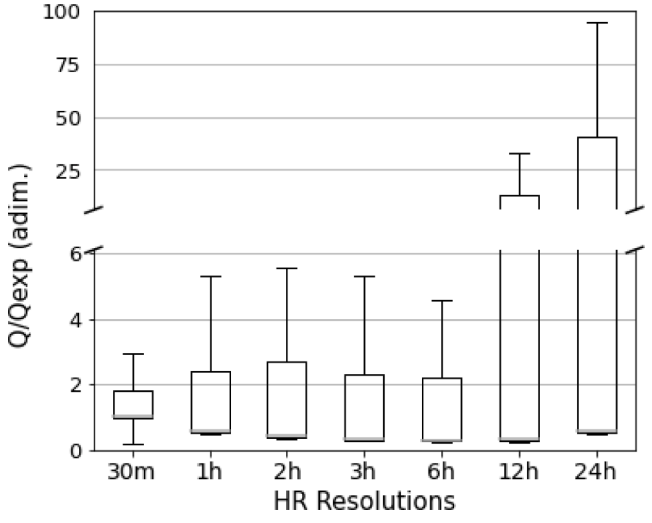

Fig. 5. Q/Q_{exp} values for all the MT-PMF experiments of different HR time resolutions. Boxes show the Q1–Q3 range, horizontal lines show the median (horizontal line), and whiskers extend up to the 1.5*IQR range (IQR = Q3-Q1).

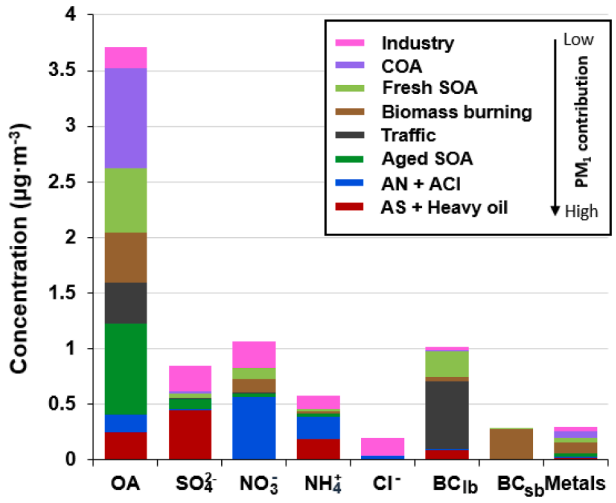

Fig. 6. Concentrations of OA (organic aerosol), SO_4^{2-}, NO_3^-, NH_4^+, Cl^-, BC_{lb}, BC_{sb} and metals in PM_1 source apportionment.

AN + ACl. The AN + ACl source contains more than a 50%, 40%, and 10% of the total apportioned mass of NO_3^-, NH_4^+, and Cl, respectively, as can be seen from the right-axis dots in Fig. 7a. The coupling of AN and ACl in the same source is likely due to their similar time variation, limited to NH_4^+ availability and with evaporation in high-temperature conditions, even if their origin is different (NO_3^- stemming mostly from traffic, Cl^- from industry or waste incineration). It apportions the majority of NO_3^- and around a third of the NH_4^+ (Fig. 6). The seasonality of this source is marked as seen in Fig. 7b, 7e, increasing in winter months because of the higher stability of the AN compound at low temperature (Harrison and Pio, 2017). This phenomenon is also observable in its diel pattern, with a decline from 11 AM to 8 PM in summer, the hours of maximum temperature, and hence, minimum stability of the AN (Fig. S7e). The maxima of the diel cycle around 8AM both in summer and winter is a result of the transformation of the NO_x emitted from traffic into HNO_3, and the availability of NH_4^+ from the traffic (Hopke and Querol, 2022).

Aged SOA. The Aged SOA factor is comprised by 82% MO-OOA, characterised by its high contribution of the *m/z44*, a product of OA oxidation (Fig. 7a). It is the second main contributor to OA after COA, representing a 23% of the total OA mass (Fig. 6). Aged aerosol has been reported to be the major constituent of OA in Via et al. (2021). However, this PMF results apportions some *m/z44* by other factors such as the AS + Heavy oil combustion or the biomass burning, hence a higher *m/z43-to-m/z44* ratio (0.39) with respect to the 0.21 in Via et al. (2021) is expected. Its monthly cycle peaks in the late summer months, due to the ageing of SOA after summer as in the aforementioned study (Fig. 7b, 7e). Its summer diel pattern (Fig. 7e) peaks at 4 AM due to nitrogen aqueous reactions conducing SOA oxidation enhancement and at 8AM due to the entrance of inland breeze carrying aged air masses, but in winter, this source grows at sea and land breeze onset hours, due to the recirculation of this aged aerosol.

Traffic. The traffic source consists of the HOA hydrocarbon pattern from vehicle exhaust and BC_{lf} concentrations (Fig. 7a). Its time series (Fig. 7b) exhibits a significant decline in summer as in Brines et al. (2019), both due to a decrease in traffic and higher atmospheric dispersion in these months. There is also a huge peak in November (Fig. 7e) due to sustained stagnation episodes and a higher traffic intensity in this month (see Figs. S6, S9 in Via et al. (2021)). Also, huge peaks appear in the time series of this factor and others (biomass burning, fresh SOA, COA), backing the explanation of stagnant conditions, which might consequently increase significantly the monthly

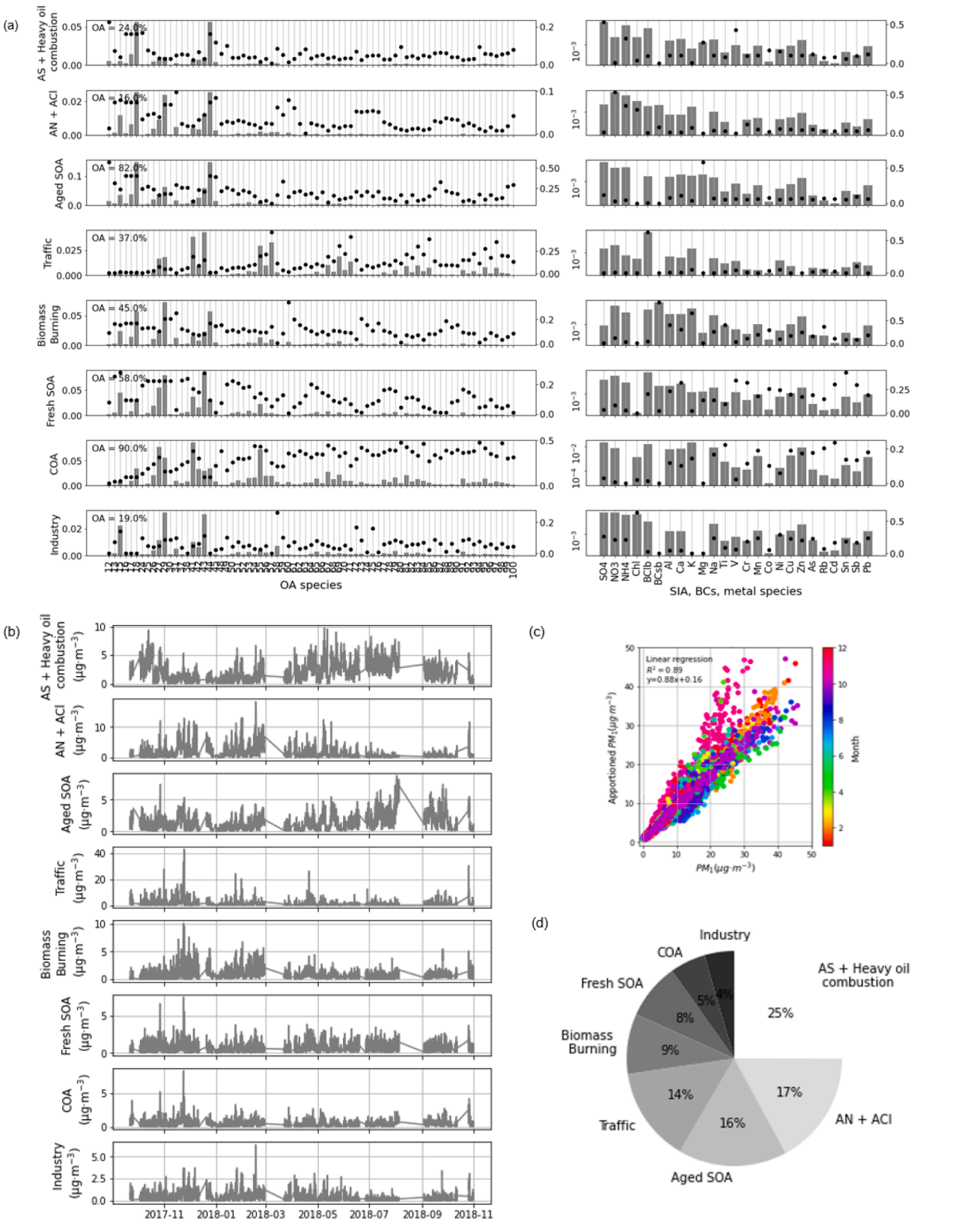

Fig. 7. Source apportionment of the multi-time resolution optimised PMF. (a) Profiles. (b) Time series (c) Mass closure (d) Pie of apportionment (e) Monthly and diel cycles. For the profiles plot (a), bars (left axis) show the normalised concentrations of each species in each factor, circles (right axis) show the percentage of each species attributed to each factor, and percentages show the proportion of OA to the total mass of that factor. Also, the left panel is dedicated to the unit-mass-resolution OA species and the right one (in log scale) to the rest of the species. The mass closure scatter plot (c) depicts the relationship between the apportioned PM_1 mass as a sum of all factors' concentrations vs. the input PM_1 mass coloured by months. Note that in (e) y-axis for the monthly means does not start at zero for more clarity in the values variation.

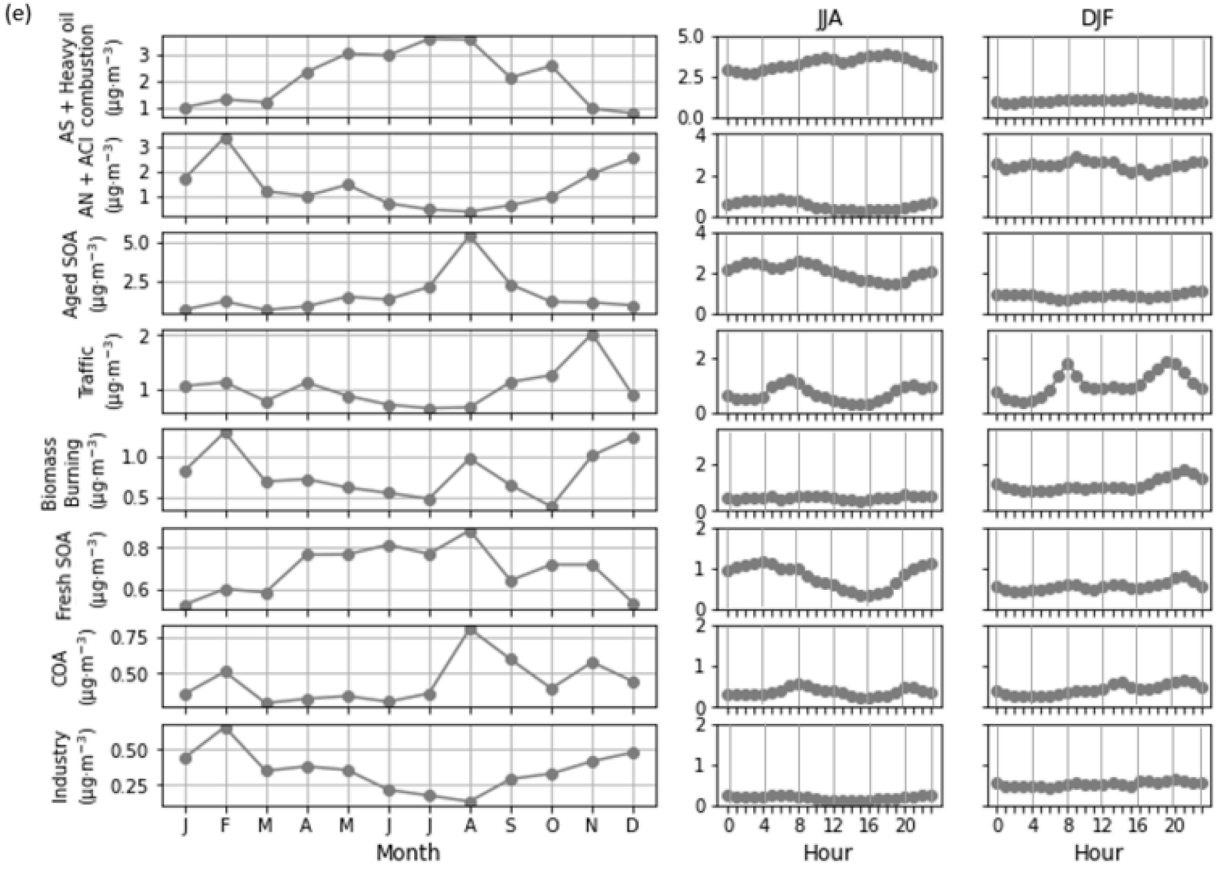

Fig. 7. (*continued*).

average. This source represents the main contribution to the total BC_{lf} (Fig. 6). However, a larger fraction of this source would be expected in the first months of the year, similarly to November and December (Fig. 7e). The proportion of traffic emissions in this study (14%, Fig. 7d) is similar to that reported by Brines et al. (2019) (14%) and slightly lower than in Amato et al. (2016); In't Veld et al. (2021) (20% and 32%, respectively, in $PM_{2.5}$). The traffic diel cycle presents two peaks, more marked in winter, around 7–8 AM and 6–8 PM (Fig. 7e), coinciding with the hours of higher traffic intensity near the site as seen in Figure S9 of Via et al. (2021).

Biomass burning. The biomass burning profile (Fig. 7a) has a high concentrations of *m/z60* and *m/z73*, organic markers of cellulose combustion (Alfarra et al., 2007; Hu et al., 2013), a high proportion of BC_{sf}, and K, a biomass burning metal tracer (Gilardoni et al., 2009; Zhao et al., 2020). This source apportions most of the BC_{sf} and a significant proportion of the NO_3^- and NH_4^+ species (Fig. 6), since AN concentrations are especially high during winter stagnation conditions coincidingly with biomass burning high levels (Reche et al., 2012), hence PMF resolves them slightly mixed. Anyhow, presence of nitrate in this source is expected as organonitrates have been reported to be related to biomass burning (Schurman et al., 2015; Yazdani et al., 2021). Its apportionment of a ~ 15% of *m/z44*, substantially higher than that from *m/z43* entails that this source is rather oxidised. Its relative contribution is similar to those from previous studies (a 14% in Brines et al. (2019), Fig. 7d). The time series of this factor is significantly higher in winter months (Fig. 7e). In the same figure, the winter diel cycle can be observed to present its maximum at evenings, suggesting this source is increased when: i. land breeze returning inland pollutants that originate from agricultural areas and rural areas burning wood for heating; ii. pollutant advection from residential heating reaching the site. The summer diel cycle is very flat due to the low concentrations.

Fresh SOA. The fresh SOA factor is composed of LO-OOA in a 58% (Fig. 7d) and apportioning a 16% of the total OA mass (Fig. 6), containing its typical pattern of C_xH_yO hydrocarbons (Fig. 7a). Its *m/z43*-to-*m/z44* ratio is 2.75, substantially higher than that found for the same period in Via et al., (2021), 1.05, since the majority of *m/z44* has been attributed to other sources as aforementioned. For the purpose of SOA description, a more differentiated OOA aerosol in terms of oxidation state (as found here with respect to the aforementioned study) can further reveal the origins of each of them due to the increased disentanglement. This difference is a consequence of the apportionment of more *m/z44* by other sources (BBOA, AS + heavy oil combustion, AN + AC), which makes sense since these sources can also be aged and share certain cyclicity related to recirculation of pollutants. This factor also apportions certain mass to BC_{lb} (around a 17%, Fig. 6) a 10% of the apportioned NO_3^- and some road dust markers (Sn, Sb, Cu, Fig. 7a). The contributions imply that this SOA formation could have been promoted by traffic emissions. It also contains other metals likely linked to industry (Cd, Ni, Cr), due to a certain entanglement with this factor. The monthly cycle showed a growth towards warm months (even disregarding August) as a consequence of a higher SOA formation due to a higher photochemical activity. In winter, the diel pattern is relatively constant and it presents slight peaks during the traffic hours. Conversely, the summer diel is minimal during the midday hours due to the higher photo-oxidation of this pollutant (and conversion into a more oxidised aerosol), the widening of the mixing layer, and the evaporation of AN due to the higher temperatures during the day.

COA. The COA factor is composed a 90% of a COA profile, containing the main cooking marker ions such as *m/z55, m/z41, m/z69, m/z29,* amongst others (Fig. 7a), and accounting for around a 24% of the total OA (Fig. 6). Although this factor is almost purely OA, it also contains certain markers in a low proportion of mineral dust and industry markers (Ti, Mn, Rb, Cd, Pb, Fig. 7a), containing around a 25% of the total metals concentrations (Fig. 6). A possible reason for this factor

including industrial, road dust, and mineral markers is that this source does not only consist of cooking emissions but on an urban ensemble of pollutants being locally recirculated. This factor does not contain a clear seasonality, but its diel cycle presents consistent peaks around 8AM, 13 and 20 PM, typical cooking times in Barcelona (Fig. 7b, 7e). This lunch peak is more evident in summer since in winter this factor is likely entangled with the traffic factor given that it peaks during the traffic rush hours (7–8 AM), which makes the noon peak less obvious. This factor accounts for a 5% of the total mass of PM_1 (Fig. 7d).

Industry. The industrial factor contributes to 4% of the total mass (Fig. 7d) and accounts for 80% of the total Cl^- mass (Fig. 7a). The apportionment of Cl^- in industrial source has been found in other industrial profiles (Brines et al., 2019; Vossler et al., 2016). Only 19% of its mass is attributed to OA (Fig. 7a), whose pattern contains mainly *m/z58*, and *m/z86*, reported industrial markers (Ge et al., 2011). These ions, related to amines, can originate from waste incineration (Leach et al., 1999), which is probably partially responsible for Cl^- emissions and was reported T the site in Brines et al. (2019). Moreover, amine production from marine emissions is not discarded. This source also incorporates high concentrations of Na, Mn, Cu, Zn, Ni, As, Pb, related to metallurgic industrial activities (Querol et al., 2007). This is coherent with previous studies reported industrial sources at this site, being characterised by the same fine inorganic species (Amato et al., 2016; Brines et al., 2019; In't Veld et al., 2021). Also, the high Cl^- and Na concentrations are not expected to be mainly from marine emissions since sea salt in the fine fraction is rather low in Barcelona, the wind rose does not point to the location of the sea (Fig. S10), and the variation of the concentrations shows no relation with the coarse fraction (Fig S11). This factor presents a descent in the warm months, probably due to an enhanced boundary layer height in the warmer periods (Fig. 7e). The diel cycle is generally flat and in summer months, a decrease can be observed as a consequence of the boundary layer widening (Fig. 7e).

3.6. PMF approaches comparison

To assess the added value of the MTR-PMF technique, its results were compared to other SA methodologies solutions. SA was also performed on the HR data subset (Approach 1), the LR data subset with only the offline species (Approach 2), a pseudo-conventional data subset (Approach 3), and an unweighted low TR base case (Approach 4) (Fig. 8). The SA of Approach 2 and Approach 3 retrieved only 4 sources, although with different fingerprints. This difference was driven by the included species. The source resolution performed by PMF can be substantially different and of more or less environmental feasibility. While the offline LR data subset SA led to the identification of road dust, it was unable to identify a road traffic source corresponding to exhaust emissions, as the data subset lacks the tracer species for that. For the pseudo-conventional data subset SA, the identified sources were mixed in some cases, which is a known limitation of this type of datasets. The clearest example is the source that included biomass burning and AN together, which are two separated factors in Approach 5 (although crossed influence is still noticeable). Additionally, it distributed quite equally the OA and EC in all factors. None of these SA results was able to identify a COA factor due to the lack of COA tracers or diel cycle, as Approach 2 only considers metal species, and Approach 3 includes OA a bulk single species and both present low TR. The base case (Approach 4) comprised all OA *m/z*s, SIA species, differentiated BC species, all averaged to the LR TR, and metals, naturally at this TR. Even though it merges different instrumentation data, no uncertainty weightings were applied, as we want to use these results to assess the final MTR result, which includes the uncertainty weightings as one of its improvements. The base case SA resulted in 6 sources, as it includes information from a wider range of species. Aged SOA + AS was differentiated from Aged SOA + heavy oil, as opposed to the results from the HR SA, which was unable to separate them. However, the AN source and fresh SOA were not separated in this approach and neither were the COA and HOA factors, the latters being clearly separated in the HR SA.

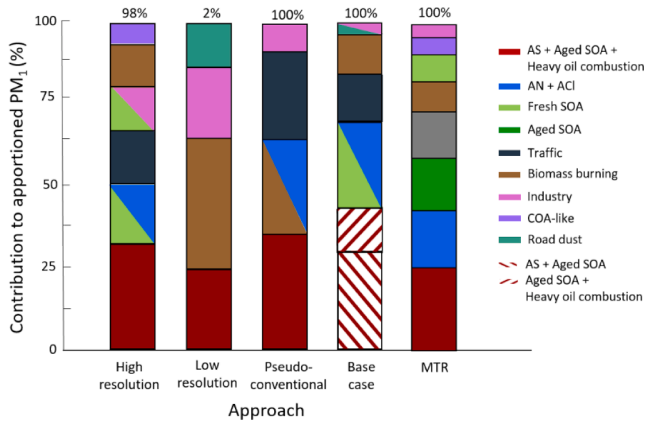

Fig. 8. Summary of source apportionment results of all input PMF datasets. Percentages at the top of each bar represent the fraction of the PM1 mass that each data subset contains depending on the species it contains. In the base case the split of factors is represented as wefted bars.

The capacity of the MTR-PMF SA for identifying and quantifying sources has been found superior to that of any of the other assessed approaches. Hence, it managed to retrieve 8 different sources, which is four more than the LR dataset or the pseudo-conventional data subset, and two more if compared to the HR data subset or the base case. The MTR-PMF merges two major advantages that cannot be applied together otherwise: a) the use of a high number of species analysed by different techniques and/or collected from the atmosphere by different methods and b) the use of the best available TR for a given species. Note that the TR can be determined by the analytical technique or by the sample collection technique; i.e. filter samples could be collected every 12 h and the dataset time resolution would be improved while applying the same analytical techniques, provided the concentrations were high enough to remain above detection limits. Thus, advantage a) would lead us from solution of Approach 1, of Approach 2 or of Approach 3 to the solution of the base case (Approach 4). Advantage b) applied independently would just give us the solution in Approach 1, where we can use the original time resolution without any restriction. The application of MTR-PMF allows the merging of both advantages and leads us from solution of base case (Approach 4) to the MTR-PMF solution.

The intra-day patterns, stemming from the use of HR TR measurements, provided significant insights into the behaviour of the sources and even enabled the identification of some sources such as COA. The comparison with the HR solution highlights the beneficial capacity of the MTR-PMF to identify more sources due to the inclusion of the metals, which are markers for some sources (heavy oil combustion, industry, biomass burning). Another advantage is the capability to match both HR and LR markers of a source resulting in a more comprehensive source description (e.g. BBOA coupled with BC_{sb}, K; OA with amine markers, likely from industrial emissions, coupled with industry markers; road traffic OA coupled with Sb). This coupling also made infer that the origin of fresh SOA could be related to traffic emissions. In addition, the MTR-PMF technique also provided separated sources for factors that had been mixed to others in the previous Approaches, isolating for example the AN from the fresh SOA. Besides, The MTR-PMF is capable to provide profiles containing mostly one kind of data and giving little mass to the rest (e.g. COA mainly containing OA; or AN + ACl and industry containing mainly non-OA measurements (<20% of OA).

4. Conclusions

A comprehensive source apportionment (SA) of the submicron particulate matter (PM_1) has been performed coupling Quadrupole Aerosol Chemical Speciation Monitor (Q-ACSM), aethalometer (AE33) and

quartz-fibre filter measurements. The species used in this SA consisted on the organic mass spectra, SO_4^{2-}, NO_3^-, NH_4^+, and Cl^- from Q-ACSM at a 30 min time resolution (TR); black carbon (BC) speciated into BC liquid fuel (BC_{lf}) and BC solid fuel (BC_{sf}) from aethalometer at 30 min TR; and metal species (Ca, Al, K, Mg, Na, Ti, V, Cr, Mn, Co, Ni, Cu, Zn, As, Sn, Sb, Pb) from offline samples at a TR of 24 h every 4th day. The use of the Positive Matrix Factorisation (PMF) model for the ensemble of the so-called high-resolution data subset (HR, 30-minutes TR) and the low-resolution data subset (LR, 24 h every 4th day TR) taken together implied the use of the multi-time resolution (MTR) PMF.

The main outcomes from this work are:

- The extended practice of averaging the high TR data subsets to reduce the TR difference with the lower TR data subsets or even to match it has been proven disadvantageous for model performance and error minimisation as also reported by Kuo et al. (2014) and Liao et al. (2013). High TRs do not represent noise to PMF since stable, robust sources are retrieved profiting the 30 min TR for disentangling sources. For instance, the COA, which was only resolved by using high TR data since its diel cycle is vital for its differentiation.
- The use of a greater number of species has enabled the characterisation of specific sources traced by key species not present in all datasets. This is the case, for instance, of the inclusion of industrial markers, which have enabled the characterisation of the industry source, whose description with only OA, SIA and BC species would have been less conclusive.
- The MTR-PMF provided an environmentally reasonable PM_1 SA with more speciated and detailed sources with respect to the other approaches and previous studies in the area using simpler SA methodologies, even if they contain longer time series or if they contain a greater number of species.
- Coherent matches of OA fingerprints and SIA, BC, and metal species were found in the MTR-PMF solution. e.g. BBOA with BC_{sb}, K; HOA with BC_{lf}, Sb; LO-OOA with AN; industry metal markers with Cl, *m/z58*, *m/z86*, etc.
- The $F_{overlap}$ method for weighting uncertainties proposed by Tong et al. (2022) does not necessarily lead to the most environmentally reasonable solution. The investigation of other runs whose $F_{overlap}$ is similar to $F^*_{overlap}$ is advisable to obtain the best SA.

To the authors' knowledge, this is the first study that applies MTR-PMF aiming to provide an exhaustive PM_1 SA assessing both the uncertainty weighting and TR SA impacts. Further research should aim to standardise these assessments to be able to include all kinds of instrument measurements to retrieve more powerful SA results aimed for both modelling and health research and mitigation policy enforcements.

Code availability

The codes used for the data analysis can be obtained upon request to the corresponding author.

Data availability

The subsets can be found in https://doi.org/10.17632/xfv7z6jzcm.1 and https://doi.org/10.17632/skp8szjhc3.1.

5. Financial support

The present work was supported by European Union's Horizon 2020 research and innovation programme under grant agreement 101,036,245 (RI-URBANS); the "Agencia Estatal de Investigación" from the Spanish Ministry of Science, Innovation and Universities, and FEDER funds under the projects CAIAC (PID2019-108990RB-I00) and HOUSE (CGL2016-78594-R); and the Generalitat de Catalunya (AGAUR 2017 SGR41) and the Direcció General de Territori.

CRediT authorship contribution statement

Marta Via: Conceptualization, Methodology, Validation, Formal analysis, Investigation, Resources, Data curation, Writing – original draft, Writing – review & editing, Visualization. **Jesús Yus-Díez:** Software, Resources, Investigation, Data curation, Writing – review & editing. **Francesco Canonaco:** Conceptualization, Methodology, Validation, Investigation, Writing – review & editing. **Jean-Eudes Petit:** Conceptualization, Writing – review & editing. **Philip Hopke:** Methodology, Validation, Writing – review & editing. **Cristina Reche:** Resources, Data curation, Writing – review & editing. **Marco Pandolfi:** Software, Resources, Investigation, Data curation, Writing – review & editing. **Matic Ivančič:** Resources, Writing – review & editing. **Martin Rigler:** Resources, Writing – review & editing. **André S.H. Prevôt:** Writing – review & editing. **Xavier Querol:** Conceptualization, Writing – review & editing, Supervision, Project administration, Funding acquisition. **Andrés Alastuey:** Conceptualization, Methodology, Validation, Resources, Writing – review & editing, Supervision, Project administration, Funding acquisition. **María Cruz Minguillón:** Conceptualization, Methodology, Validation, Formal analysis, Data curation, Resources, Writing – review & editing, Supervision, Project administration, Funding acquisition.

Declaration of Competing Interest

The authors declare that they have no known competing financial interests or personal relationships that could have appeared to influence the work reported in this paper.

Data availability

Data will be made available on request.

Acknowledgements

We acknowledge support of the COST Action CA16109 COLOSSAL. IDAEA-CSIC is a Centre of Excellence Severo Ochoa (Spanish Ministry of Science and Innovation, grant no. CEX2018-000794-S). We would like to thank Aerosol d.o.o. for lending the AE33 aethalometer.

Appendix A. Supplementary material

Supplementary data to this article can be found online at https://doi.org/10.1016/j.envint.2023.108006.

References

Agrawal, H., Eden, R., Zhang, X., Fine, P.M., Katzenstein, A., Miller, J.W., Ospital, J., Teffera, S., Cocker, D.R., 2009. Primary particulate matter from ocean-going engines in the Southern California Air Basin. Environ. Sci. Technol. 43 (14), 5398–5402. https://doi.org/10.1021/es8035016.

Alfarra, M.R., Prevot, A.S.H., Szidat, S., Sandradewi, J., Weimer, S., Lanz, V.A., Schreiber, D., Mohr, M., Baltensperger, U., 2007. Identification of the mass spectral signature of organic aerosols from wood burning emissions. Environ. Sci. Technol. 41 (16), 5770–5777. https://doi.org/10.1021/es062289b.

Allan, J.D., Delia, A.E., Coe, H., Bower, K.N., Alfarra, M.R., Jimenez, J.L., Middlebrook, A.M., Drewnick, F., Onasch, T.B., Canagaratna, M.R., Jayne, J.T., Worsnop, D.R., 2004. A generalised method for the extraction of chemically resolved mass spectra from Aerodyne aerosol mass spectrometer data. J. Aerosol Sci. 35 (7), 909–922. https://doi.org/10.1016/j.jaerosci.2004.02.007.

Amato, F., Alastuey, A., Karanasiou, A., Lucarelli, F., Nava, S., Calzolai, G., Severi, M., Becagli, S., Gianelle, V.L., Colombi, C., Alves, C., Custódio, D., Nunes, T., Cerqueira, M., Pio, C., Eleftheriadis, K., Diapouli, E., Reche, C., Minguillón, M.C., Manousakas, M.I., Maggos, T., Vratolis, S., Harrison, R.M., Querol, X., 2016. AIRUSE-LIFE+: a harmonized PM speciation and source apportionment in five southern European cities. Atmos. Chem. Phys. 16 (5), 3289–3309. https://doi.org/10.5194/acp-16-3289-2016.

Belis, C.A., Pikridas, M., Lucarelli, F., Petralia, E., Cavalli, F., Calzolai, G., Berico, M., Sciare, J., 2019. Source apportionment of fine PM by combining high time resolution organic and inorganic chemical composition datasets. Atmos. Environ. X 3, 100046. https://doi.org/10.1016/j.aeaoa.2019.100046.

Brines, M., Dall'Osto, M., Amato, F., Minguillón, M.C., Karanasiou, A., Grimalt, J.O., Alastuey, A., Querol, X., van Drooge, B.L., 2019. L.: Source apportionment of urban PM1 in Barcelona during SAPUSS using organic and inorganic components. Environ.

Sci. Pollut. Res. 26 (31), 32114–32127. https://doi.org/10.1007/s11356-019-06199-3.
Canonaco, F., Tobler, A., Chen, G., Sosedova, Y., Slowik, J.G., Bozzetti, C., Daellenbach, K.R., El Haddad, I., Crippa, M., Huang, R.-J., Furger, M., Baltensperger, U., Prévôt, A.S.H., 2021. A new method for long-term source apportionment with time-dependent factor profiles and uncertainty assessment using SoFi Pro: application to 1 year of organic aerosol data. Atmos. Meas. Tech. 14 (2), 923–943. https://doi.org/10.5194/amt-14-923-2021.
Caumette, G., Lienemann, C.P., Merdrignac, I., Bouyssiere, B., Lobinski, R., 2009. Element speciation analysis of petroleum and related materials. J. Anal. At. Spectrom. 24 (3), 263–276. https://doi.org/10.1039/b817888g.
Cavalli, F., Viana, M., Yttri, K.E., Putaud, J.P., Genberg, J., Putaud, J.-P., 2010. Toward a standardized thermal-optical protocol for measuring atmospheric organic and elemental carbon: the eusaar protocol, ACS, Div. Environ. Chem. - Prepr. Ext. Abstr. 48 (1), 443–446. https://doi.org/10.5194/amtd-2-2321-2009.
Corbin, J.C., Mensah, A.A., Pieber, S.M., Orasche, J., Michalke, B., Zanatta, M., Czech, H., Massabò, D., Buatier De Mongeot, F., Mennucci, C., El Haddad, I., Kumar, N.K., Stengel, B., Huang, Y., Zimmermann, R., Prévôt, A.S.H., Gysel, M., 2018. Trace metals in soot and PM2.5 from heavy-fuel-oil combustion in a marine engine. Environ. Sci. Technol. 52 (11), 6714–6722. https://doi.org/10.1021/acs.est.8b01764.
Crenn, V., Sciare, J., Croteau, P.L., Verlhac, S., Fröhlich, R., Belis, C.A., Aas, W., Äijälä, M., Alastuey, A., Artiñano, B., Baisnée, D., Bonnaire, N., Bressi, M., Canagaratna, M., Canonaco, F., Carbone, C., Cavalli, F., Coz, E., Cubison, M.J., Esser-Gietl, J.K., Green, D.C., Gros, V., Heikkinen, L., Herrmann, H., Lunder, C., Minguillón, M.C., Močnik, G., O'Dowd, C.D., Ovadnevaite, J., Petit, J.E., Petralia, E., Poulain, L., Priestman, M., Riffault, V., Ripoll, A., Sarda-Estève, R., Slowik, J.G., Setyan, A., Wiedensohler, A., Baltensperger, U., Prévôt, A.S.H., Jayne, J.T., Favez, O., 2015. ACTRIS ACSM intercomparison - Part 1: reproducibility of concentration and fragment results from 13 individual Quadrupole Aerosol Chemical Speciation Monitors (Q-ACSM) and consistency with co-located instruments. Atmos. Meas. Tech. 8 (12), 5063–5087. https://doi.org/10.5194/amt-8-5063-2015.
Crespi, A., Bernardoni, V., Calzolai, G., Lucarelli, F., Nava, S., Valli, G., Vecchi, R., 2016. Implementing constrained multi-time approach with bootstrap analysis in ME-2: an application to PM2.5 data from Florence (Italy). Sci. Total Environ. 541, 502–511. https://doi.org/10.1016/j.scitotenv.2015.08.159.
Crippa, M., Canonaco, F., Slowik, J.G., El Haddad, I., Decarlo, P.F., Mohr, C., Heringa, M. F., Chirico, R., Marchand, N., Temime-Roussel, B., Abidi, E., Poulain, L., Wiedensohler, A., Baltensperger, U., Prévôt, A.S.H., 2013. Primary and secondary organic aerosol origin by combined gas-particle phase source apportionment. Atmos. Chem. Phys. 13 (16), 8411–8426. https://doi.org/10.5194/acp-13-8411-2013.
Drinovec, L., Močnik, G., Zotter, P., Prévôt, A.S.H., Ruckstuhl, C., Coz, E., Rupakheti, M., Sciare, J., Müller, T., Wiedensohler, A., Hansen, A.D.A., 2015. The "dual-spot" Aethalometer: an improved measurement of aerosol black carbon with real-time loading compensation. Atmos. Meas. Tech. 8 (5), 1965–1979. https://doi.org/10.5194/amt-8-1965-2015.
Escrig Vidal, A., Monfort, E., Celades, I., Querol, X., Amato, F., Minguillón, M.C., Hopke, P.K., 2009. Application of optimally scaled target factor analysis for assessing source contribution of ambient PM10. J. Air Waste Manag. Assoc. 59 (11), 1296–1307. https://doi.org/10.3155/1047-3289.59.11.1296.
Forello, A.C., Bernardoni, V., Calzolai, G., Lucarelli, F., Massabò, D., Nava, S., Pileci, R.E., Prati, P., Valentini, S., Valli, G., Vecchi, R., 2019. Exploiting multi-wavelength aerosol absorption coefficients in a multi-time source apportionment study to retrieve source-dependent absorption parameters. Atmos. Chem. Phys. Discuss. 1–26 https://doi.org/10.5194/acp-2019-123.
Gangoiti, G., Millán, M.M., Salvador, R., Mantilla, E., 2001. Long-range transport and re-circulation of pollutants in the western Mediterranean during the project Regional Cycles of Air Pollution in the West-Central Mediterranean Area. Atmos. Environ. 35 (36), 6267–6276. https://doi.org/10.1016/S1352-2310(01)00440-X.
Ge, X., Wexler, A.S., Clegg, S.L., 2011. Atmospheric amines – Part I. a review. Atmospheric Environ. 45 (3), 524–546. https://doi.org/10.1016/j.atmosenv.2010.10.012.
Gilardoni, S., Liu, S., Takahama, S., Russell, L.M., Allan, J.D., Steinbrecher, R., Jimenez, J.L., De Carlo, P.F., Dunlea, E.J., Baumgardner, D., 2009. Characterization of organic ambient aerosol during MIRAGE 2006 on three platforms. Atmos. Chem. Phys. 9 (15), 5417–5432. https://doi.org/10.5194/acp-9-5417-2009.
Harrison, R. M. and Pio, C. A.: Tellus B : Chemical and Physical Meteorology An investigation of the atmospheric HNO 3 -NH 3 - NH 4 NO 3 equilibrium relationship in a cool , humid climate An investigation of the atmospheric equilibrium relationship in a cool , humid climate, , 0889(3), doi:10.3402/tellusb.v35i2.14795, 2017.
Henry, R.C., Lewis, C.W., Hopke, P.K., Williamson, H.J., 1984. Review of receptor model fundamentals. Atmos. Environ. 18 (8), 1507–1515. https://doi.org/10.1016/0004-6981(84)90375-5.
Hidy: Atmospheric sulfur and nitrogen oxides: Eastern north American source-receptor relationships., 1994.
Hopke, P.K., Querol, X., 2022. Is improved vehicular NOx control leading to increased urban NH3Emissions? Environ. Sci. Technol. 56 (17), 11926–11927. https://doi.org/10.1021/acs.est.2c04996.
Hopke, P.K., Dai, Q., Li, L., Feng, Y., 2020. Global review of recent source apportionments for airborne particulate matter. Sci. Total Environ. 740, 140091 https://doi.org/10.1016/j.scitotenv.2020.140091.
Hu, W.W., Hu, M., Yuan, B., Jimenez, J.L., Tang, Q., Peng, J.F., Hu, W., Shao, M., Wang, M., Zeng, L.M., Wu, Y.S., Gong, Z.H., Huang, X.F., He, L.Y., 2013. Insights on organic aerosol aging and the influence of coal combustion at a regional receptor site of central eastern China. Atmos. Chem. Phys. 13 (19), 10095–10112. https://doi.org/10.5194/acp-13-10095-2013.
P.L., K.: Interactions of Climate Change, Air Pollution, and Human Health, Curr. Environ. Heal. reports, 5(1), 179–186 [online] Available from: http://www.embase.com/search/results?subaction=viewrecord&from=export&id=L625310095%0Ahttps://doi.org/10.1007/s40572-018-0188-x, 2018.
Kuo, C.P., Liao, H.T., Chou, C.C.K., Wu, C.F., 2014. Source apportionment of particulate matter and selected volatile organic compounds with multiple time resolution data. Sci. Total Environ. 472, 880–887. https://doi.org/10.1016/j.scitotenv.2013.11.114.
Leach, J., Blanch, A., Bianchi, A.C., 1999. Volatile organic compounds in an urban airborne environment adjacent to a municipal incinerator, waste collection centre and sewage treatment plant. Atmos. Environ. 33 (26), 4309–4325. https://doi.org/10.1016/S1352-2310(99)00115-6.
Liao, H.T., Kuo, C.P., Hopke, P.K., Wu, C.F., 2013. Evaluation of a modified receptor model for solving multiple time resolution equations: a simulation study. Aerosol Air Qual. Res. 13 (4), 1253–1262. https://doi.org/10.4209/aaqr.2012.11.0322.
Middlebrook, A.M., Bahreini, R., Jimenez, J.L., Canagaratna, M.R., 2012. Evaluation of composition-dependent collection efficiencies for the Aerodyne aerosol mass spectrometer using field data. Aerosol Sci. Technol. 46 (3), 258–271. https://doi.org/10.1080/02786826.2011.620041.
Minguillón, M.C., Schembari, A., Triguero-Mas, M., de Nazelle, A., Dadvand, P., Figueras, F., Salvado, J.A., Grimalt, J.O., Nieuwenhuijsen, M., Querol, X., 2012. Source apportionment of indoor, outdoor and personal PM2.5 exposure of pregnant women in Barcelona, Spain. Atmospheric Environ. 59, 426–436. https://doi.org/10.1016/j.atmosenv.2012.04.052.
Minguillón, M.C., Pérez, N., Marchand, N., Bertrand, A., Temime-Roussel, B., Agrios, K., Szidat, S., van Drooge, B., Sylvestre, A., Alastuey, A., Reche, C., Ripoll, A., Marco, E., Grimalt, J.O., Querol, X., 2016. Secondary organic aerosol origin in an urban environment: influence of biogenic and fuel combustion precursors. Faraday Discuss 189, 337–359. https://doi.org/10.1039/c5fd00182j.
Mohr, C., DeCarlo, P.F., Heringa, M.F., Chirico, R., Slowik, J.G., Richter, R., Reche, C., Alastuey, A., Querol, X., Seco, R., Peñuelas, J., Jiménez, J.L., Crippa, M., Zimmermann, R., Baltensperger, U., Prévôt, A.S.H., 2012. Identification and quantification of organic aerosol from cooking and other sources in Barcelona using aerosol mass spectrometer data. Atmos. Chem. Phys. 12 (4), 1649–1665. https://doi.org/10.5194/acp-12-1649-2012.
Ng, N.L., Herndon, S.C., Trimborn, A., Canagaratna, M.R., Croteau, P.L., Onasch, T.B., Sueper, D., Worsnop, D.R., Zhang, Q., Sun, Y.L., Jayne, J.T., 2011. An Aerosol chemical speciation monitor (ACSM) for routine monitoring of the composition and mass concentrations of ambient aerosol. Aerosol Sci. Technol. 45 (7), 770–784. https://doi.org/10.1080/02786826.2011.560211.
Ogulei, D., Hopke, P.K., Zhou, L., Paatero, P., Park, S.S., Ondov, J.M., 2005. Receptor modeling for multiple time resolved species: the Baltimore supersite. Atmos. Environ. 39 (20), 3751–3762. https://doi.org/10.1016/j.atmosenv.2005.03.012.
Paatero, P., 1999. The multilinear engine—a table-driven, least squares program for solving multilinear problems, including the n-way parallel factor analysis model. J. Comput. Graph. Stat. 8 (4), 854–888.
Paatero, P., Tapper, U., 1994. Positive matrix factorization: a non-negative factor model with optimal utilization of error estimates of data values. Environmetrics 5 (2), 111–126. https://doi.org/10.1002/env.3170050203.
Passig, J., Schade, J., Irsig, R., Li, L., Li, X., Zhou, Z., Adam, T., Zimmermann, R., 2021. Detection of ship plumes from residual fuel operation in emission control areas using single-particle mass spectrometry. Atmos. Meas. Tech. 14 (6), 4171–4185. https://doi.org/10.5194/amt-14-4171-2021.
Pérez, N., Pey, J., Querol, X., Alastuey, A., López, J.M., Viana, M., 2008. Partitioning of major and trace components in PM10–PM2.5–PM1 at an urban site in Southern Europe. Atmospheric Environ. 42 (8), 1677–1691. https://doi.org/10.1016/j.atmosenv.2007.11.034.
Pérez, N., Pey, J., Reche, C., Cortés, J., Alastuey, A., Querol, X., 2016. Impact of harbour emissions on ambient PM10 and PM2.5 in Barcelona (Spain): Evidences of secondary aerosol formation within the urban area. Sci. Total Environ. 571, 237–250. https://doi.org/10.1016/j.scitotenv.2016.07.025.
Pey, J., Pérez, N., Querol, X., Alastuey, A., Cusack, M., Reche, C., 2010. Intense winter atmospheric pollution episodes affecting the Western Mediterranean. Sci. Total Environ. 408 (8), 1951–1959. https://doi.org/10.1016/j.scitotenv.2010.01.052.
Querol, X., Alastuey, A., Rodriguez, S., Plana, F., Ruiz, C.R., Cots, N., Massagué, G., Puig, O., 2001. PM10 and PM2.5 source apportionment in the Barcelona Metropolitan area, Catalonia, Spain. Atmos. Environ. 35 (36), 6407–6419. https://doi.org/10.1016/S1352-2310(01)00361-2.
Querol, X., Viana, M., Alastuey, A., Amato, F., Moreno, T., Castillo, S., Pey, J., de la Rosa, J., Sánchez de la Campa, A., Artíñano, B., Salvador, P., García Dos Santos, S., Fernández-Patier, R., Moreno-Grau, S., Negral, L., Minguillón, M.C., Monfort, E., Gil, J.I., Inza, A., Ortega, L.A., Santamaría, J.M., Zabalza, J., 2007. Source origin of trace elements in PM from regional background, urban and industrial sites of Spain. Atmos. Environ. 41 (34), 7219–7231. https://doi.org/10.1016/j.atmosenv.2007.05.022.
Reche, C., Viana, M., Amato, F., Alastuey, A., Moreno, T., Hillamo, R., Teinilä, K., Saarnio, K., Seco, R., Peñuelas, J., Mohr, C., Prévôt, A.S.H., Querol, X., 2012. Biomass burning contributions to urban aerosols in a coastal Mediterranean City. Sci. Total Environ. 427–428, 175–190. https://doi.org/10.1016/j.scitotenv.2012.04.012.
Sandradewi, J., Prévôt, A.S.H., Weingartner, E., Schmidhauser, R., Gysel, M., Baltensperger, U., 2008. A study of wood burning and traffic aerosols in an Alpine valley using a multi-wavelength Aethalometer. Atmos. Environ. 42 (1), 101–112. https://doi.org/10.1016/j.atmosenv.2007.09.034.

Schurman, M.I., Lee, T., Desyaterik, Y., Schichtel, B.A., Kreidenweis, S.M., Collett, J.L., 2015. Transport, biomass burning, and in-situ formation contribute to fine particle concentrations at a remote site near Grand Teton National Park. Atmos. Environ. 112, 257–268. https://doi.org/10.1016/j.atmosenv.2015.04.043.

Slowik, J.G., Stroud, C., Bottenheim, J.W., Brickell, P.C., Chang, R.Y.W., Liggio, J., Makar, P.A., Martin, R.V., Moran, M.D., Shantz, N.C., Sjostedt, S.J., Van Donkelaar, A., Vlasenko, A., Wiebe, H.A., Xia, A.G., Zhang, J., Leaitch, W.R., Abbatt, J.P.D., 2010a. Characterization of a large biogenic secondary organic aerosol event from eastern Canadian forests. Atmos. Chem. Phys. 10 (6), 2825–2845. https://doi.org/10.5194/acp-10-2825-2010.

Slowik, J.G., Vlasenko, A., McGuire, M., Evans, G.J., Abbatt, J.P.D., 2010b. Simultaneous factor analysis of organic particle and gas mass spectra: AMS and PTR-MS measurements at an urban site. Atmos. Chem. Phys. 10 (4), 1969–1988. https://doi.org/10.5194/acp-10-1969-2010.

Sofowote, U.M., Healy, R.M., Su, Y., Debosz, J., Noble, M., Munoz, A., Jeong, C.-H., Wang, J.M., Hilker, N., Evans, G.J., Hopke, P.K., 2018. Understanding the PM2.5 imbalance between a far and near-road location: results of high temporal frequency source apportionment and parameterization of black carbon. Atmospheric Environ. 173, 277–288. https://doi.org/10.1016/j.atmosenv.2017.10.063.

Srivastava, D., Favez, O., Petit, J.E., Zhang, Y., Sofowote, U.M., Hopke, P.K., Bonnaire, N., Perraudin, E., Gros, V., Villenave, E., Albinet, A., 2019. Speciation of organic fractions does matter for aerosol source apportionment. Part 3: combining off-line and on-line measurements. Sci. Total Environ. 690, 944–955. https://doi.org/10.1016/j.scitotenv.2019.06.378.

Tong, Y., Qi, L., Stefenelli, G., Canonaco, D. S. W. F., Baltensperger, U., Prevot, A. S. H. and Slowik1, J. G.: Quantification of primary and secondary organic aerosol sources by combined factor analysis of extractive electrospray ionisation and aerosol mass spectrometer measurements (EESI-TOF and AMS), Atmos. Meas. Tech., (March), 1–50, 2022.

Ulbrich, I.M., Canagaratna, M.R., Zhang, Q., Worsnop, D.R., Jimenez, J.L., 2009. Interpretation of organic components from Positive Matrix Factorization of aerosol mass spectrometric data. Atmos. Chem. Phys. 9 (9), 2891–2918. https://doi.org/10.5194/acp-9-2891-2009.

Veld, M.i.'t., Alastuey, A., Pandolfi, M., Amato, F., Pérez, N., Reche, C., Via, M., Minguillón, M.C., Escudero, M., Querol, X., 2021. Compositional changes of PM2.5 in NE Spain during 2009–2018: a trend analysis of the chemical composition and source apportionment. Sci. Total Environ. 795, 148728. https://doi.org/10.1016/j.scitotenv.2021.148728.

Via, M., Chen, G., Canonaco, F., Daellenbach, K. R., Chazeau, B., Chebaicheb, H., Jiang, J., Keernik, H., Lin, C., Marchand, N., Marin, C., O'Dowd, C., Ovadnevaite, J., Petit, J.-E., Pikridas, M., Riffault, V., Sciare, J., Slowik, J. G., Simon, L., Vasilescu, J., Zhang, Y., Favez, O., Prévôt, A. S. H., Alastuey, A. and Minguillón, M. C.: Rolling vs. Seasonal PMF: Real-world multi-site and synthetic dataset comparison, EGUsphere, 2022, 1–29 [online] Available from: https://egusphere.copernicus.org/preprints/egusphere-2022-269/, 2022.

Via, M., Minguillón, M.C., Reche, C., Querol, X., Alastuey, A., 2021. Increase in secondary organic aerosol in an urban environment. Atmos. Chem. Phys. 21 (10), 8323–8339. https://doi.org/10.5194/acp-21-8323-2021.

Vossler, T., Černikovský, L., Novák, J., Williams, R., 2016. Source apportionment with uncertainty estimates of fine particulate matter in Ostrava, Czech Republic using Positive Matrix Factorization. Atmos. Pollut. Res. 7 (3), 503–512. https://doi.org/10.1016/j.apr.2015.12.004.

WHO: WHO global air quality guidelines, Coast. Estuar. Process., 1–360, 2021.

Yazdani, A., Dudani, N., Takahama, S., Bertrand, A., Prévôt, A.S.H., El Haddad, I., Dillner, A.M., 2021. Characterization of primary and aged wood burning and coal combustion organic aerosols in an environmental chamber and its implications for atmospheric aerosols. Atmos. Chem. Phys. 21 (13), 10273–10293. https://doi.org/10.5194/acp-21-10273-2021.

Yus-Díez, J., Bernardoni, V., Močnik, G., Alastuey, A., Ciniglia, D., Ivančič, M., Querol, X., Perez, N., Reche, C., Rigler, M., Vecchi, R., Valentini, S., Pandolfi, M., 2021. Determination of the multiple-scattering correction factor and its cross-sensitivity to scattering and wavelength dependence for different AE33 Aethalometer filter tapes: a multi-instrumental approach. Atmos. Meas. Tech. Discuss. 29, 1–30. https://doi.org/10.5194/amt-2021-46.

Zhao, H., Wakil, M.A., Viljanen, J., Song, Q., Yao, Q., Kwong, C.W., Alwahabi, Z.T., 2020. In situ measurement of potassium release during biomass combustion using laser-induced breakdown spectroscopy: effect of silicate on potassium release. Energy and Fuels 34 (3), 3262–3271. https://doi.org/10.1021/acs.energyfuels.9b03966.

Zhou, L., Hopke, P.K., Paatero, P., Ondov, J.M., Pancras, J.P., Pekney, N.J., Davidson, C. I., 2004. Advanced factor analysis for multiple time resolution aerosol composition data. Atmos. Environ. 38 (29), 4909–4920. https://doi.org/10.1016/j.atmosenv.2004.05.040.

Zografou, O., Gini, M., Manousakas, M.I., Chen, G., Kalogridis, A.C., Diapouli, E., Pappa, A., Eleftheriadis, K., 2022. Combined organic and inorganic source apportionment on yearlong ToF-ACSM dataset at a suburban station in Athens. Atmos. Meas. Tech. 15 (16), 4675–4692. https://doi.org/10.5194/amt-15-4675-2022.

Zotter, P., Herich, H., Gysel, M., El-Haddad, I., Zhang, Y., Mocnik, G., Hüglin, C., Baltensperger, U., Szidat, S., Prévôt, A.S.H., 2017. Evaluation of the absorption Ångström exponents for traffic and wood burning in the Aethalometer-based source apportionment using radiocarbon measurements of ambient aerosol. Atmos. Chem. Phys. 17 (6), 4229–4249. https://doi.org/10.5194/acp-17-4229-2017.